UC Irvine
UC Irvine Previously Published Works

Title
Photochemistry of Thin Solid Films of the Neonicotinoid Imidacloprid on Surfaces

Permalink
https://escholarship.org/uc/item/5563n2df

Journal
Environmental Science and Technology, 51(5)

ISSN
0013-936X

Authors
Aregahegn, Kifle Z
Shemesh, Dorit
Gerber, R Benny
et al.

Publication Date
2017-03-07

DOI
10.1021/acs.est.6b04842

Peer reviewed

Photochemistry of Thin Solid Films of the Neonicotinoid Imidacloprid on Surfaces

Kifle Z. Aregahegn,[†] Dorit Shemesh,[‡] R. Benny Gerber,*,[†,‡] and Barbara J. Finlayson-Pitts*,[†]

[†]Department of Chemistry, University of California, Irvine, California 92697, United States

[‡]Department of Physical Chemistry and the Fritz Haber Research Center, The Hebrew University, Jerusalem 91904, Israel

S *Supporting Information*

ABSTRACT: Imidacloprid (IMD) is the most widely used neonicotinoid insecticide found on environmental surfaces and in water. Analysis of surface-bound IMD photolysis products was performed using attenuated total reflectance Fourier transfer infrared (ATR-FTIR) analysis, electrospray ionization (ESI-MS), direct analysis in real time mass spectrometry (DART-MS), and transmission FTIR for gas-phase products. Photolysis quantum yields (ϕ) for loss of IMD were determined to be $(1.6 \pm 0.6) \times 10^{-3}$ (1s) at 305 nm and $(8.5 \pm 2.1) \times 10^{-3}$ (1s) at 254 nm. The major product is the imidacloprid urea derivative (IMD-UR, 84% yield), with smaller amounts of the desnitro-imidacloprid (DN-IMD, 16% yield) product, and gaseous nitrous oxide (N_2O). Theoretical calculations show that the first step of the main mechanism is the photodissociation of NO_2, which then recombines with the ground electronic state of IMD radical to form IMD-UR and N_2O in a thermally driven process. The photolytic lifetime of IMD at a solar zenith angle of 35° is calculated to be 16 h, indicating the significant reaction of IMD over the course of a day. Desnitro-imidacloprid has been identified by others as having increased binding to target receptors compared to IMD, suggesting that photolysis on environmental surfaces increases toxicity.
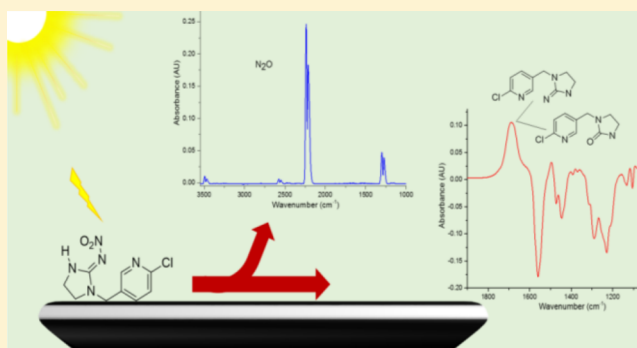
INTRODUCTION

Neonicotinoid (NN) insecticides, which represent one-third of the total world insecticide market,[1] are widely used to control sucking insect pests.[1−3] They are applied as aqueous solutions or oil dispersions to different substrates including seeds, soil, and foliage and even directly to cats and dogs for flea control.[3] As a result, they are found on a variety of surfaces in the environment.[4−6] Neonicotinoids selectively bind to nicotinic acetylcholine receptors as the primary target for pest control[3,7−11] and are believed to have low toxicity to nontarget species.[12,13] However, there is increasing concern about possible adverse effects of NN on invertebrates,[14] vertebrates,[15] pollinators (especially bees),[16−19] birds,[20] and humans,[21] and they are regulated by the European Union but not yet by the U.S. Environmental Protection Agency (EPA).[22]

Once in the environment, insecticides undergo photochemical and thermal reactions that lead to the formation of products whose toxicity can differ from that of the parent compound. For example, malathion sprayed over Southern California to control the Mediterranean fruit fly was shown to oxidize rapidly on surfaces in air to form malaoxon, which has a much larger oral toxicity to rats than malathion.[23]

Imidacloprid (1-[(6-chloropyridin-3-yl)methyl]-*N*-nitroimidazolidin-2-imine, IMD) is the most widely used neonicotinoid[3] and has been detected in different plants[24] and in human urine.[25] A number of laboratory studies have been conducted on the photolysis of IMD, and its possible photoproducts,[26−37] and quantum yields (ϕ) have been reported for solutions.[27,31,37] In most studies, the desnitro derivative (1-[(6-chloropyridin-3-yl)methyl]imidazolidin-2-imine, DN-IMD) is the major product.[27−29,35−37] Smaller yields of the urea derivative (1-[(6-chloropyridin-3-yl)methyl]imidazolidin-2-one, IMD-UR) are commonly observed, along with a number of minor products. Similar products have been observed from photolysis of IMD on surfaces such as tomato leaves[30] and glass Petri dishes.[28] A typical mechanism leading to the DN-IMD and IMD-UR is shown in Scheme S1.[28]

The goals of this work was to determine the rate constants (k_p), quantum yield (ϕ), products and mechanisms of photolysis of IMD on surfaces. Photolysis was carried out using broadband radiation centered at 305 nm, as well as 254 nm narrowband radiation. To the best of our knowledge, this is the first report quantitative measurement of quantum yields for photolysis of solid IMD on surfaces and the first identification and measurement of the gaseous products. Theoretical calculations were carried out that elucidate the initial steps in photolysis as well as secondary chemistry in the cage provided

by the solid matrix that leads to the observed gas-phase and solid products.

EXPERIMENTAL SECTION

Thin layers of IMD were prepared by atomizing (TSI, model no. 3076) a solution of IMD (Fluka, PESTANALRTM, 99.9%) in acetonitrile (ACS grade, 99.5%) onto the top surface of a clean germanium (Ge) ATR crystal (Pike Technologies, 45°, 80 mm × 10 mm × 4 mm) to give a coated surface area of ~4 cm². The sample was dried in open air for a minimum of 30 min and then placed in a custom-built ATR reaction cell[38] (Figure S1 and section 2 in the Supporting Information). The cell contains gas inlets and outlets, a horizontally mounted quartz window on the top, and zinc selenide end windows (ZnSe, Edmund Optics, 10 mm diameter ×1.5 mm thickness). The sample on the crystal was irradiated through the top quartz window. Infrared spectra (128 scans, 4 cm⁻¹ resolution) were recorded (Mattson Galaxy 5020 FTIR) before and during irradiation. The loss of IMD and formation of surface-bound products under a flow of dry nitrogen or air (Praxair) were followed using ATR-FTIR. The residence time of the gas flow in the reaction cell based on the volume of the cell (17 cm³) and the flow rate (~100 cm³ min⁻¹) is ~10 s. The depth of penetration[39] (d_p) of the evanescent wave from the Ge-ATR crystal to air, which is appropriate for thin films, was 0.15−0.69 μm over the 4000−860 cm⁻¹ wavenumber range. To probe the gas phase, an ATR spectrum was taken before photolysis, and then the cell was repositioned in the spectrometer so that the IR beam passed through the gas phase above the ATR crystal; in this case, the gas inlets and outlets were closed so there was no gas flow through the cell during photolysis. Gas-phase spectra were measured with time, and at the end of the photolysis, the cell was repositioned to measure the final ATR spectrum.

To convert the measured IMD absorbance to absolute numbers of molecules, ATR-FTIR spectra were also measured for IMD in acetonitrile solutions at varying concentrations. In this case, the evanescent wave penetrates into the bulk, which was much thicker than the depth of penetration; the effective thickness (d_e) that was probed for the solutions was calculated using Ge to acetonitrile indices of refraction[39] to be 0.13−0.59 μm over the same wavenumber range. From d_e and the known solution concentration, the number of IMD molecules probed were calculated and used to estimate the number probed in the thin film. During IMD photolysis experiments, the maximum number of IMD molecules irradiated on the ATR crystal was 9 × 10¹⁶ molecules cm⁻². Based on a unit cell volume for IMD crystals of 1108 Å³ with four molecules per unit cell,[40] it was determined that the maximum thickness for an evenly dispersed film would be 0.25 μm. This is smaller than the depth of penetration at 1565 cm⁻¹, d_p = 0.4 μm, that was followed with time to obtain photolysis rate constants, so that the entire film was in principle interrogated. Inhomogeneities in the film were inevitable so some parts were above the depth of penetration; however, 90% or more of the IMD signal typically decreased at long photolysis times, suggesting that most, if not all, of the film was probed.

Absorption spectra of IMD and the major photolysis products, IMD-UR and DN-IMD, were measured as described in Figure S2, Table S1, and section 3 in the Supporting Information. Photolysis was carried out using either a low-pressure mercury lamp (UVP, CPQ-5851) with a line at 254 nm or a low-pressure organic phosphor coated mercury lamp

(Jelight, 84-2061-2), which has a broadband emission from 285 to 360 nm with mercury lines superimposed as shown in Figure S3. In the latter case, a Pyrex glass coverslip was used to filter out light below 290 nm. The temperature rose to a maximum of 34 °C during photolysis. This does not affect the chemistry because it was shown in separate experiments that heating the system to 40 °C did not result in loss of the IMD or formation of products. The relative intensities of the lamp were converted to absolute photon fluxes using the photoisomerization of 2-nitrobenzaldehyde (2-NB) to 2-nitrosobenzoic acid as a chemical actinometer.[41−45] Details are given in section 4 of the Supporting Information. The results were combined with measured IMD photolysis rate constants (Figure S5 and section 4 of the Supporting Information) to obtain photolysis quantum yields (Table S2 and section 4 of the Supporting Information).

For additional product analysis, drops of the IMD solution were placed on metal screens (stainless steel, 74 Mesh 0.094 mm diameter) and photolyzed for different lengths of time. Products were analyzed by mass spectrometry (Xevo TQS, Waters) equipped using a commercial direct analysis in real time (DART) ion source described elsewhere[46,47] or an electrospray ionization (ESI) ion source. Briefly, the DART-ion source (IonSense, DART SVP with Vapur Interface) was directed toward the mass analyzer orifice at a 180° relative angle with a 5 mm sample space (Figure S6 and section 5 of the Supporting Information). Helium reagent gas (3.1 L min⁻¹) was introduced into the discharge chamber, in which metastable helium atoms (He*) were produced. The DART-ion source was operated at a gas temperature of 350 °C and a grid electrode voltage of 350 V. Mass spectra were collected in the positive-ion mode, where [M + H]⁺ are the major peaks. The screen held IMD samples before and after selected photolysis times and was moved through the DART ionization region to collect spectra for each sample (Figure S6 and section 5 of the Supporting Information).

For ESI-MS analysis, samples were extracted from the screens using a 50/50% (v/v) nanopure water (18 MΩ-cm)−methanol (99.9%, OmniSolv) solvent mixture. The ESI source was operated in positive ion mode with a capillary voltage of 3.2 kV, a desolvation gas flow of 1000 L h⁻¹, and a desolvation gas temperature of 500 °C. Peaks corresponding to [M + H]⁺ with some contribution from sodium adducts, [M + Na]⁺, were observed. Spectra were background-subtracted using MassLynx software for both ESI-MS and DART-MS.

Desnitro-imidacloprid (Fluka, Germany, 99.9%) and IMD-UR (ChemService, 98.6%) were used as standards for calibration of the products in ATR-FTIR, DART-MS, and ESI-MS. Calibration for gas-phase N₂O was performed by measuring its transmission IR absorbance at 2237 cm⁻¹ for mixtures of N₂O (Praxair, 99.9%) in air (Praxair, Ultra zero) in the reaction cell.

The error cited throughout is the standard deviation s defined by $s = \sqrt{\dfrac{\Sigma_1^N (x - \bar{x})^2}{N}}$, where N represents the number of samples.

THEORETICAL APPROACH AND THEORETICAL CALCULATIONS

To assist with interpretation of the experimental results, theoretical model calculations were also carried out. These involve several stages. A total of four low-energy conformers of IMD with relative energies within 5 kJ mol⁻¹ were recently

predicted.[48] The conformer used in the excitation calculations is depicted in Figure 1. First, calculations of optimized
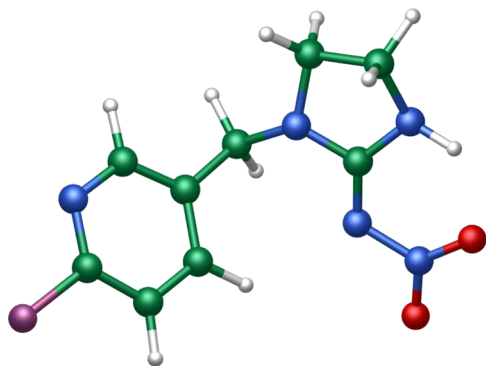
Figure 1. MP2/cc-pVDZ optimized structure of the IMD-1a conformer.

geometries, vertical excitation energies and the intensities of the transitions were performed at the level of the isolated molecule at two different levels. Accurate ab initio calculations were done using the ADC(2) method[49] using the cc-pVDZ basis set.[50] Additionally calculations were performed with the semiempirical OM2/MRCI method.[51] The OM2/MRCI method was used subsequently for the molecular dynamics simulations because the ADC(2) method is too cost-intensive and molecular dynamics simulations employing this method-ology is not feasible. The OM2/MRCI method does not have parameters for chlorine. The calculations with the OM2/MRCI were therefore performed on IMD with F substituted for Cl. These calculations were validated against ADC(2) for the fluorine compound. The electronic excitation properties were similar for chlorine and fluorine compounds (see section 6 and Tables S3−S5 in the Supporting Information), supporting the use of the fluorine compound as a model for IMD in the semiempirical calculations. Additionally, the comparison of the electronic properties computed by the semiempirical method are supported by the ab initio ADC(2) method, despite some discrepancies in the order of the excited states.

Next, molecular dynamics of the photochemistry following excitation were carried out using the semiempirical OM2/MRCI method. A similar approach was already successfully used on several systems.[52−56] Calculations with ab initio methods such as ADC(2), are not feasible at this time. The simulations correspond to an excitation at 254 nm and are performed on a single molecule. Structures were sampled from a molecular dynamics simulation of ca. 160 ps length on the ground electronic state (with a time-step of 0.1 fs) using the OM2 potential.[57] The four low-lying conformers mentioned above were accessed in the simulation. A total of 100 geometries were sampled from the ground-state dynamics and promoted to the first excited state of strong absorption cross-section. The molecular dynamics simulations were performed on the excited state using the OM2/MRCI potential for about 100 ps (with a time-step of 0.1 fs). The calculations, as will be discussed later, show two different chemical mechanisms, the major one being photodissociation of NO_2 on the subpicosecond time scale and the minor one showing a loss of the OH group.

However, it became obvious that these calculations cannot account for the experimental finding that N_2O, not NO_2, is the gas-phase product. We emphasize again that the calculations

were performed on a single molecule, whereas the experiment was performed in a solid film. The assumption of a cage effect seems, therefore, very reasonable. We assume that following photodissociation, the photofragments are trapped by the environment and also that the system returns to the ground state, resulting in recombination. Return to the ground state creates a hot species. Further calculations using molecular dynamics on the ground state using the hot molecule were not performed because this would require very long time scale simulations. We therefore carried out approximate calculations of the subsequent reaction pathways using the semiempirical OM2 method. As will be seen later, these calculations of the initial photochemistry followed by a thermal recombination process provide a satisfactory account of the experimental finding.

■ RESULTS AND DISCUSSION

Photolysis Rate Constants and Quantum Yields. The ATR-FTIR spectrum of initial IMD is shown in Figure 2a
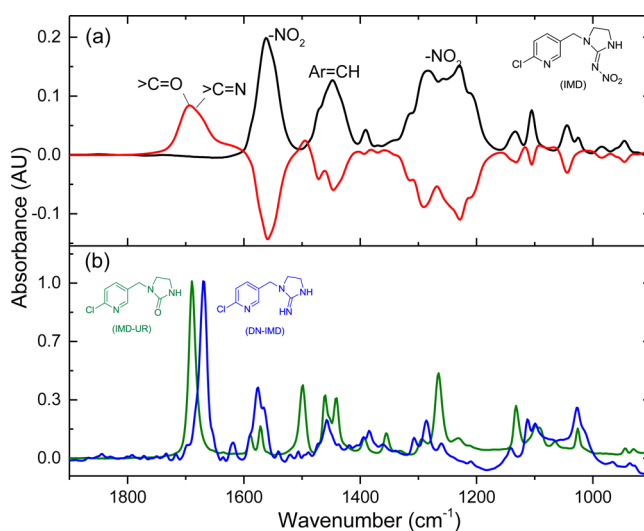
Figure 2. ATR-FTIR spectra of (a) imidacloprid in the dark (black) and the difference spectrum after 20 min of 254 nm lamp exposure of imidacloprid (red). The difference spectrum is $\log(S_0/S_1)$, where S_0 is the single beam spectrum before photolysis, and S_1 is that after photolysis. (b) Desnitro-imidacloprid (blue) and imidacloprid-urea (green) standards are shown.

(black). The $-NO_2$ group has characteristic absorption bands in the 1200−1300 cm^{-1} and 1530−1630 cm^{-1} regions due to symmetric and asymmetric vibrations of the $-NO_2$ group.[58] Bands in the region between 1350 and 1500 cm^{-1} are from aromatic C═C and C═N ring in-plane vibrations and deformation modes of ═CH− on the pyridine ring.[58] The difference spectrum after 20 min irradiation at 254 nm (Figure 2a, red), shows negative peaks that reflect loss of the parent IMD and positive peaks from newly formed products (imidacloprid exposed to a flow of air in the reaction cell for 12 h in the dark showed no loss). Upon irradiation, the bands due to the $-NO_2$ group in IMD decrease, and a new broad band appears at ∼1690 cm^{-1}. As discussed below, this is indicative of the loss of $-NO_2$ from IMD. As reported for studies in solution,[27−30,32] and explored in more detail below, two major products of IMD photolysis are DN-IMD and IMD-UR (compounds 2 and 3 in Scheme S1, respectively). Figure 2b shows that both of these products have infrared absorption

bands in the 1650−1750 cm^{-1} region where the new band from IMD photolysis appears.

As shown in Figure S2, IMD absorbs UV light out to ~340 nm, and photolysis of IMD under 254 or 305 nm irradiation follows first-order kinetics (Figure S5). The average values for the photolysis rate constants at 254 and 305 nm light are $(1.6 \pm 0.4) \times 10^{-3}$ and $(1.5 \pm 0.5) \times 10^{-5}$ (1s), respectively. As described in the Supporting Information, the photolysis rate constants were used along with measurements of absolute light intensities based on 2-NB as an actinometer to obtain photolysis quantum yields (ϕ_λ) for loss of IMD, which are also shown in Table S2. The quantum yields at the two wavelengths are $\phi_{254 \text{ nm}} = (8.5 \pm 2.1) \times 10^{-3}$ (1s) and $\phi_{305 \text{ nm}} = (1.6 \pm 0.6) \times 10^{-3}$ (1s).

To the best of our knowledge, this is the first measurement of the quantum yields of IMD on surfaces. For comparison, quantum yields reported in the literature for photolysis in aqueous solutions are shown in Table 1. The value measured

**Table 1. Comparison of Quantum Yields (ϕ) of Imidacloprid at Different Wavelengths**

wavelength range	experimental conditions	ϕ ($\times 10^{-3}$)[a]	reference
254 nm lamp	ATR crystal	8.5 ± 2.1	this work
305 nm lamp	ATR crystal	1.6 ± 0.6	this work
xenon lamp	natural water	0.6 ± 0.03	Redlich et al.[27]
290−400 nm	borate buffer solution	15.1	Von Gunten[31]
natural sunlight	borate buffer solution	5.5	Von Gunten[31]
290−400 nm	borate buffer solution	9.2 ± 0.5	Lu et al.[37]

[a]Errors are ±1s.

here at 305 nm is smaller than that of Lu et al.[37] and von Gunten[31] but larger than that from Redlich et al.[27] Smaller quantum yields in the solid may reflect a more-efficient cage effect compared to the solution, regenerating IMD.

Based on actinic flux estimates,[59] the lifetime for IMD at the Earth's surface at a solar zenith angle of 35° corresponding to noon at 40°N latitude in early April is determined to be 16 h (see section 7 of the Supporting Information). The products IMD-UR and DN-IMD do not absorb significantly at wavelengths above 290 nm (Figure S2 and section 3 of the Supporting Information), the actinic cutoff at the Earth's surface. Thus, these IMD products, once formed, are expected to be stable with respect to further photolysis in the atmosphere.

Identification of Photolysis Products. As seen from the IR spectra in Figure 2, the new bands observed by ATR-FTIR suggest that products could include a combination of IMD-UR and DN-IMD, which have been observed in previous studies of photolysis in solutions[26−28,31−37] or on the surface of tomato plants or glass.[29,30] Figure 3a,b,e,f shows ESI (+) and DART (+) mass spectra, respectively, of IMD before photolysis and after 10 and 15 min of 254 nm irradiation; similar results were obtained at 305 nm. The products with peaks at m/z = 211/213 and 212/214 increased with irradiation time, with the ratios within each pair indicative of a chlorine isotope pattern. Dechlorination was not apparent in any of the experiments, although this has been reported for halopyridines.[60] A comparison with mass spectra of IMD-UR and DN-IMD (Figure 3c,d,g,h) shows that the photolysis product peaks are consistent with a combination of IMD-UR and DN-IMD.
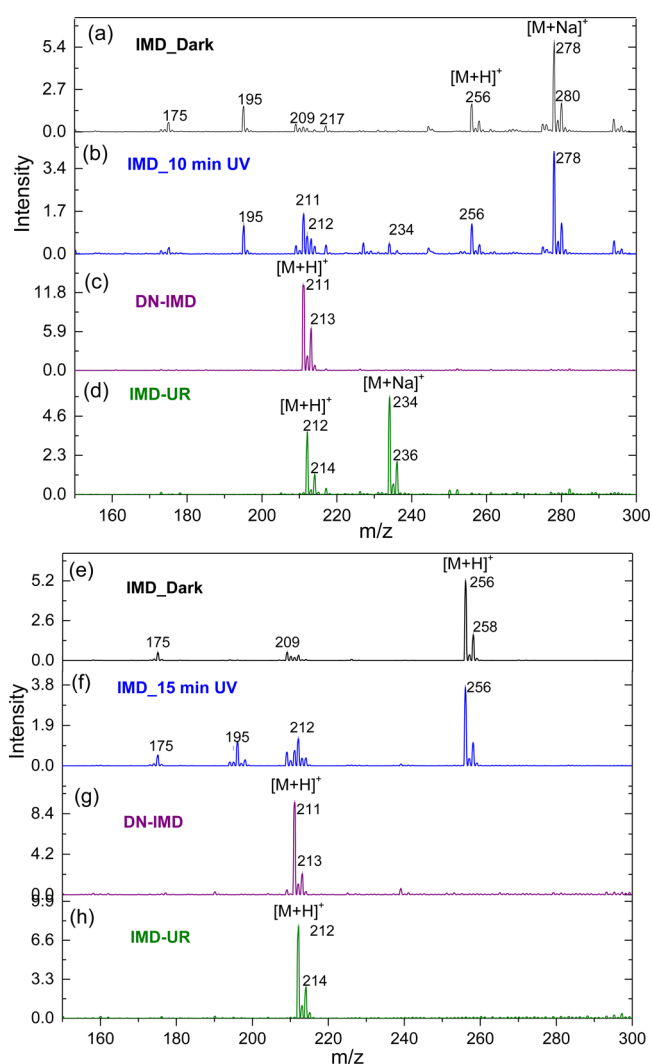
Figure 3. ESI-MS (+) spectra for: (a) imidacloprid in the dark, (b) imidacloprid after 10 min of 254 nm irradiation, (c) authentic desnitro-imidacloprid, and (d) authentic imidacloprid urea. DART-MS (+) spectra for: (e) imidacloprid in the dark, (f) imidacloprid after 15 min of 254 nm irradiation, (g) authentic desnitro-imidacloprid, and (h) an authentic imidacloprid urea sample. The m/z 195 and 217 peaks in ESI and m/z 195 in DART are due to caffeine added as a standard.

Relative sensitivities for the two products by DART-MS and ESI-MS were determined by obtaining mass spectra of mixtures prepared in known concentration ratios (Figure S7 and section 8A in the Supporting Information). Detailed summaries can be found in Table S6. Within experimental error, there is no significant trend with photolysis time. For DART-MS, the average molar ratio of IMD-UR to DN-IMD is 5.6 ± 0.5 (1s), while for ESI-MS, the average is 5.2 ± 1.0 (1s), where the averages are over both wavelengths. In short, the IMD-UR is the major photolysis product (84%), with smaller amounts (16%) of DN-IMD also being produced. This differs from most reports of products from solution-phase photolysis[27,28,35,37,61] and on tomato plants or glass[28,29] where DN-IMD was reported to be the major product (a few report IMD-UR as the major product).[30,32,34]

Transmission FTIR of the gas phase above IMD on the ATR crystal showed peaks at 3482, 2223, and 1285 cm^{-1}, which, by comparison to an authentic standard, is identified as nitrous

oxide, N_2O (Figure S8). Neither NO_2 nor NO were observed. This is the first identification of the gas-phase products, and N_2O in particular, during IMD photolysis. The N_2O yields, $\Delta N_2O/\Delta IMD$, are summarized in Table 2 (details can be found in Table S7 and section 8 of the Supporting Information. The average is 0.88 ± 0.26 (1s) at 305 nm and 0.53 ± 0.10 (1s) at 254 nm.

Table 2. Average Molar Ratio of IMD-UR to DN-IMD and Nitrous Oxide Yields from Imidacloprid Direct Photolysis on a Ge ATR Crystal at 305 and 254 nm

| lamp (nm)	average molar ratio of [IMD-UR] to [DN-IMD]		average $\Delta[N_2O]/\Delta[IMD]^a$
	ESI-MS[a]	DART-MS[a]	
305	4.3 ± 0.2	5.2 ± 0.4	0.88 ± 0.26
254	6.0 ± 0.4	6.1 ± 0.1	0.53 ± 0.10

[a]Errors are $\pm$1s.

Photolysis Mechanism. The proposed reaction mechanism for photolysis of IMD and formation of the surface-bound and gas-phase products is given in Scheme 1. The mechanism is based on the experimental observations and insight provided by the theoretical calculations (see section 9 of the Supporting Information).

The initial optimized geometry for IMD (Figure 1) has the main atoms of the six-membered ring in one plane, whereas most of the other atoms are in a second plane, tilted by about 110° relatively to the first plane. The hydrogen of the NH

group is hydrogen bonded to the oxygen of the NO_2 group. Excitation energies for the chlorine and fluorine compounds with the ab initio method ADC(2) and the semiempirical OM2/MRCI method are given in Tables S3−S5. Briefly, the transition with the highest oscillator strength as predicted with the semiempirical method involves a $\pi\pi^*$ transition (from the HOMO π orbital on the six-membered ring to the LUMO π^* orbital on the rings and NO_2 group) and is energetically accessible at 254 nm.

According to our calculations of the vertical excitation energy, there seem to be no corresponding transitions that match the experimental excitation at the longer, 305 nm, wavelength. However, the calculations were carried out only for one conformer. The most likely mechanism for this absorption is participation of other conformers that are higher in energy, which are not accounted for in the structure calculations. Additionally, the calculations were done on a single molecule, whereas in the experiment the molecule is surrounded by other molecules. The environment can affect the transition energy. Thus, in our opinion, the Franck−Condon region in reality is likely to include more-energetic structures for which the Franck−Condon excitation energy is lower. Alternatively, theory predicts a transition at 3.9 eV (Table S3) but with a much smaller oscillator strength. Although the dynamics were not studied for the latter case, alkyl nitrates are known to photolyze above 300 nm to generate NO_2,[62] so it is likely that cleavage to generate NO_2 also occurs with the broadband 305 nm lamp. Recombination would result in less energy in the recombination species but still enough to overcome the barriers

Scheme 1. Proposed Photolysis Mechanism of Imidacloprid on the ATR Crystal
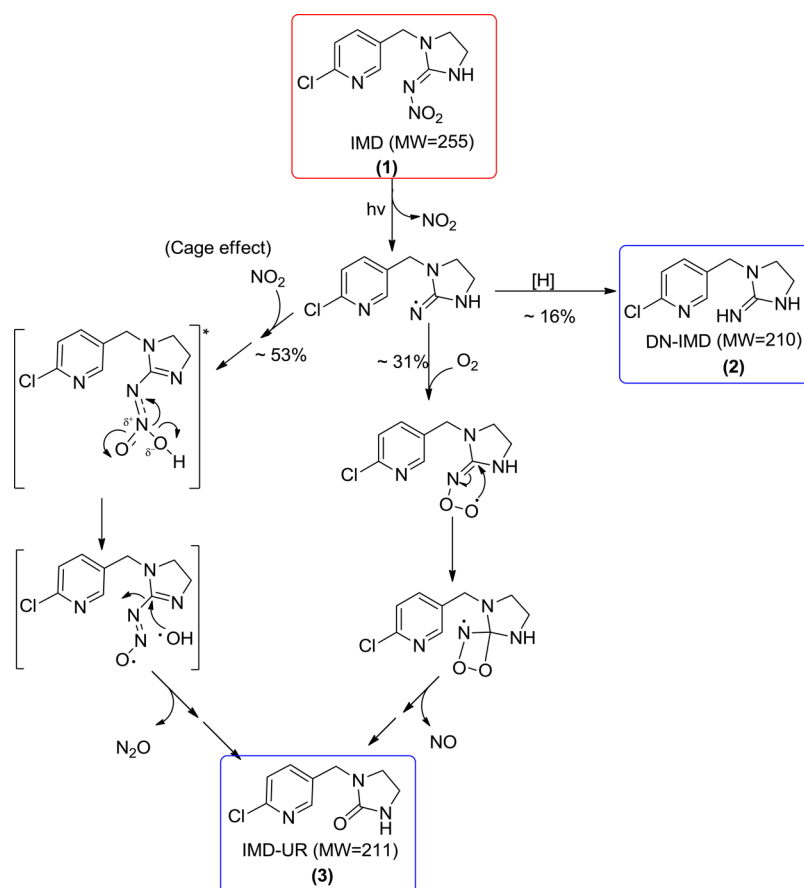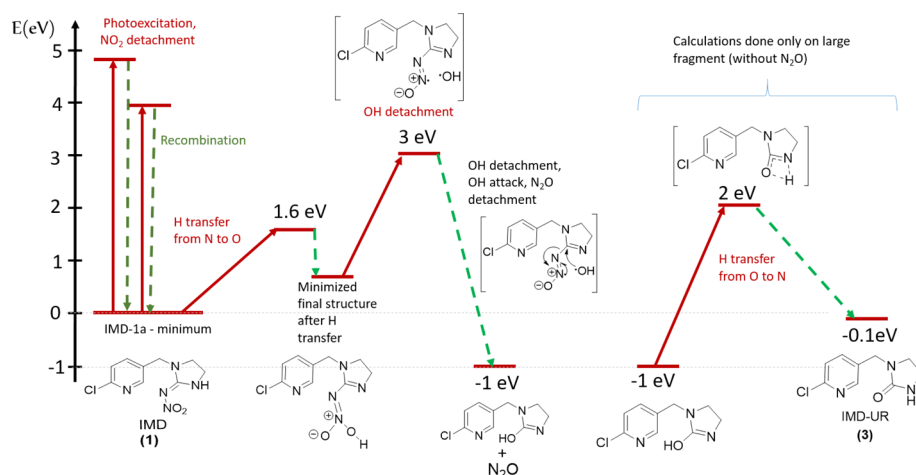
Figure 4. Energetics of the initial excitation and the subsequent reactions of IMD photolysis. Arrows serve to indicate both transfers of electrons into and from bonds and chemical reactions.

in Figure 4. The smaller quantum yield for the loss of IMD at 305 nm is consistent with less energy available when NO_2 recombines with the organic radical, leading to more-efficient recombination to reform IMD. In short, the excitation energy agrees reasonably well with experiment.

A pair of important reaction pathways are observed in the excited-state dynamics. First, in about 2% of the trajectories (see Figure S10), the H from the NH group is transferred to the oxygen of the NO_2 group, and in a second step, the OH is detached. The large fragment is left with a N_2O moiety attached. A possible next step (not observed) would be the detachment of N_2O. This pathway is consistent with a minor channel for producing the experimentally detected N_2O. The carbonyl containing large fragment can be explained by an attack of the previously detached OH radical (assuming a cage effect due to the environment) and a transfer of the hydrogen back to the nitrogen to which it was originally connected.

The theory predicts that 83% of the trajectories release NO_2 rather than the experimentally observed N_2O. However, the simulation is performed on a single molecule, whereas the experiment is performed in a solid film. It is therefore reasonable to assume a cage effect that leads to the recombination of the NO_2 with the imidacloprid fragment on the electronic ground state. We therefore calculated approximate reaction paths on the potential energy surface to describe the processes that occur. The energetics of the initial excitation and the subsequent reactions are shown in Figure 4. First, the excitation energy of 4.9 eV is converted to internal energy of the molecule on recombination of the NO_2 with the organic fragment. This energy is redistributed throughout the molecule in the ground electronic state. In the next step, a hydrogen is transferred from the ring nitrogen to the oxygen of NO_2 on the ground electronic state. The barrier height is only 1.6 eV, much less than the energy released during the recombination. After optimization of the geometry, the next step is cleavage of the N−O bond to form OH, which requires 2 eV relative to the optimized structure. The OH then attacks the ring carbon, releasing N_2O in a process (Figure S9) that is exothermic (about 4 eV). Finally, transfer of the hydrogen from −OH back to the ring nitrogen, which has a barrier of ∼3 eV, generates the urea derivative as the solid-phase product. In short, the proposed mechanism involves several barriers that are not

higher than 3 eV and can be easily overcome by the excess energy of about 5 eV released in the NO_2 recombination event.

The energetics of this pathway are consistent with the photochemical and thermal energies available to the molecule, and the final products are in accord with the experiment. This explains in a satisfactory way why no NO_2 but rather N_2O is formed. The result of this process is the displacement of the N_2O and the formation of a carbonyl group containing second compound, as can be seen in Scheme 1. The theoretical scheme accounts reasonably well for the photon absorption and the excitation energies, as well as the subsequent dynamics of the reactions. The photochemical step, while very brief, provides the energy that drives the processes in the subsequent thermal recombination part. No attempt to model a triplet-state photodisssociation process was made. In the framework of the model used, a triplet-based mechanism is highly unlikely. The singlet-state primary process is over in less than 20 ps, much less than the time-scale estimated for conversion to the triplet.

The photolysis mechanism summarized in Scheme 1 indicates that if NO_2 cleavage and recombination represented the sole pathway, then equal amounts of IMD-UR and N_2O should be generated. This is the case, within experimental error, for the broadband 305 nm radiation, but the yields of N_2O are smaller at 254 nm (Table 2). It may be that the extra energy at 254 nm results in a less-efficient cage effect and, hence, less-efficient net recombination of the NO_2. In this case, the IMD radical formed on NO_2 detachment would undergo other reactions such as interacting with molecular oxygen in the gas flow to form additional IMD-UR, as shown in Scheme 1 and proposed for solution photochemistry.[27,28,32] Our mechanism for formation of DN-IMD is similar to that proposed in solution,[27,28,32] but that for IMD-UR is different in that a nitroso intermediate is not invoked because we have no evidence it is generated under our experimental conditions. Rather, recombination of NO_2 with the organic radical fragment followed by the steps described above are proposed to form IMD-UR and, simultaneously, N_2O.

The gas-phase product N_2O is a potent greenhouse gas,[59] with a global warming potential on a 20 year time scale of 264 relative to CO_2.[63] It is also a major contributor to stratospheric ozone depletion.[64] Global production of imidacloprid in 2010 was estimated to be 20 000 tons year^{-1},[1] which is equivalent to

7.8×10^7 moles year^{-1} of IMD. Assuming all of the imidacloprid produced is applied and photolyzes with an N$_2$O yield of 0.88, the annual production of N$_2$O from IMD photolysis will be 1.9 Gg year^{-1} as nitrogen. This is a small percentage of the total annual estimated human-associated (postindustrial) N$_2$O emissions of 6.5 Tg N year^{-1}.[65] However, it could have site-specific effects such as skewing measurements of N$_2$O fluxes in agricultural regions if there is an unrecognized contribution from neonicotinoid photolysis in areas where there is significant use of these insecticides. It may also be comparable in magnitude to the generation of N$_2$O via abiotic reactions of ammonium nitrate fertilizer, which has been estimated to be responsible for 5.9 Gg N per year over North America.[66] Finally, this estimate does not take into account potential contributions from other neonicotinoids containing the $-NO_2$ group, such as thiamethoxam, nitenpyram, clothianidin, and dinotefuran, which also absorb light in the actinic region and will likely be additional sources of N$_2$O.

In most solution experiments, DN-IMD is the major product and the IMD-UR is a smaller contributor; proposed mechanisms commonly involve the formation of the nitroso compound as an intermediate (compound 4 in Scheme S1). It is clear from the present studies that loss of NO$_2$ is the major initial pathway on surfaces, with formation of IMD-UR and N$_2$O through subsequent reactions in the solid matrix dominating the chemistry. Although the DN-IMD is formed in smaller yields on surfaces than in solution, it can be important because of its higher binding to nicotinic acetylcholine receptor sites, which is an indicator of mammalian toxicity.[10]

■ ASSOCIATED CONTENT

Ⓢ Supporting Information

This material is available free of charge on the ACS publications Web site. The Supporting Information is available free of charge on the ACS Publications website at DOI: 10.1021/acs.est.6b04842.

> Additional details on the reaction mechanism, materials and methods, theoretical and rate calculations, photolysis product yields, and photochemistry statistics. Figures showing UV−vis absorption cross-sections, relative emission spectra and absolute intensities, typical first-order decays of IMD, photolysis rate constants and quantum yields, a schematic for DART-MS analysis, FTIR transmission spectra, and a molecular view of the mechanism of IMD photolysis. (PDF)

■ AUTHOR INFORMATION

Corresponding Authors

*For theory, e-mail bgerber@uci.edu (R.B.G.).
*For experiment, e-mail bjfinlay@uci.edu (B.J.F.P.); phone: (949) 824-7670.

ORCID Ⓞ

Barbara J. Finlayson-Pitts: 0000-0003-4650-168X

Notes

The authors declare no competing financial interest.

■ REFERENCES

(1) Simon-Delso, N.; Amaral-Rogers, V.; Belzunces, L. P.; Bonmatin, J. M.; Chagnon, M.; Downs, C.; Furlan, L.; Gibbons, D. W.; Giorio, C.; Girolami, V.; Goulson, D.; Kreutzweiser, D. P.; Krupke, C. H.; Liess, M.; Long, E.; McField, M.; Mineau, P.; Mitchell, E. A. D.; Morrissey, C. A.; Noome, D. A.; Pisa, L.; Settele, J.; Stark, J. D.; Tapparo, A.; Van Dyck, H.; Van Praagh, J.; Van der Sluijs, J. P.; Whitehorn, P. R.; Wiemers, M. Systemic insecticides (neonicotinoids and fipronil): trends, uses, mode of action and metabolites. *Environ. Sci. Pollut. Res.* **2015**, *22* (1), 5−34.

(2) Elbert, A.; Haas, M.; Springer, B.; Thielert, W.; Nauen, R. Applied aspects of neonicotinoid uses in crop protection. *Pest Manage. Sci.* **2008**, *64* (11), 1099−1105.

(3) Jeschke, P.; Nauen, R.; Schindler, M.; Elbert, A. Overview of the status and global strategy for neonicotinoids. *J. Agric. Food Chem.* **2011**, *59* (7), 2897−2908.

(4) Obana, H.; Okihashi, M.; Akutsu, K.; Kitagawa, Y.; Hori, S. Determination of neonicotinoid pesticide residues in vegetables and fruits with solid phase extraction and liquid chromatography mass spectrometry. *J. Agric. Food Chem.* **2003**, *51* (9), 2501−2505.

(5) Stewart, S. D.; Lorenz, G. M.; Catchot, A. L.; Gore, J.; Cook, D.; Skinner, J.; Mueller, T. C.; Johnson, D. R.; Zawislak, J.; Barber, J. Potential exposure of pollinators to neonicotinoid insecticides from the use of insecticide seed treatments in the mid-southern united states. *Environ. Sci. Technol.* **2014**, *48* (16), 9762−9769.

(6) Anderson, J. C.; Dubetz, C.; Palace, V. P. Neonicotinoids in the Canadian aquatic environment: A literature review on current use products with a focus on fate, exposure, and biological effects. *Sci. Total Environ.* **2015**, *505*, 409−422.

(7) Ihara, M.; Matsuda, K.; Shimomura, M.; Sattelle, D. B.; Komai, K. Super Agonist Actions of Clothianidin and Related Compounds on the SADβ; Nicotinic Acetylcholine Receptor Expressed in Xenopus laevis Oocytes. *Biosci., Biotechnol., Biochem.* **2004**, *68* (3), 761−763.

(8) Ihara, M.; Brown, L. A.; Ishida, C.; Okuda, H.; Sattelle, D. B.; Matsuda, K. Actions of imidacloprid, clothianidin and related neonicotinoids on nicotinic acetylcholine receptors of American cockroach neurons and their relationships with insecticidal potency. *J. Pestic. Sci.* **2006**, *31* (1), 35−40.

(9) Matsuda, K.; Buckingham, S. D.; Kleier, D.; Rauh, J. J.; Grauso, M.; Sattelle, D. B. Neonicotinoids: insecticides acting on insect nicotinic acetylcholine receptors. *Trends Pharmacol. Sci.* **2001**, *22* (11), 573−580.

(10) Chao, S. L.; Casida, J. E. Interaction of Imidacloprid Metabolites and Analogs with the Nicotinic Acetylcholine Receptor of Mouse Brain in Relation to Toxicity. *Pestic. Biochem. Physiol.* **1997**, *58*, 77−88.

(11) Tomizawa, M.; Casida, J. E. Neonicotinoid insecticide toxicology: mechanisms of selective action. *Annu. Rev. Pharmacol. Toxicol.* **2005**, *45* (1), 247−268.

(12) CalEPA, Department of Pesticide Regulation. Imidacloprid: Risk Characterization Document: Dietary and Drinking Water Exposure; California Environmental Protection Agency: Sacramento, CA, 2006.

(13) Matsuda, K.; Kanaoka, S.; Akamatsu, M.; Sattelle, D. B. Diverse actions and target-site selectivity of neonicotinoids: structural insights. *Mol. Pharmacol.* **2009**, *76* (1), 1−10.

(14) van der Sluijs, J. P.; Amaral-Rogers, V.; Belzunces, L. P.; Bijleveld van Lexmond, M. F. I. J.; Bonmatin, J.-M.; Chagnon, M.; Downs, C. A.; Furlan, L.; Gibbons, D. W.; Giorio, C.; Girolami, V.; Goulson, D.; Kreutzweiser, D. P.; Krupke, C.; Liess, M.; Long, E.; McField, M.; Mineau, P.; Mitchell, E. A. D.; Morrissey, C. A.; Noome, D. A.; Pisa, L.; Settele, J.; Simon-Delso, N.; Stark, J. D.; Tapparo, A.; Van Dyck, H.; van Praagh, J.; Whitehorn, P. R.; Wiemers, M. Conclusions of the Worldwide Integrated Assessment on the risks of neonicotinoids and fipronil to biodiversity and ecosystem functioning. *Environ. Sci. Pollut. Res.* **2015**, *22* (1), 148−154.

(15) Gibbons, D.; Morrissey, C.; Mineau, P. A review of the direct and indirect effects of neonicotinoids and fipronil on vertebrate wildlife. *Environ. Sci. Pollut. Res.* **2015**, *22* (1), 103−118.

(16) Rundlof, M.; Andersson, G. K. S.; Bommarco, R.; Fries, I.; Hederstrom, V.; Herbertsson, L.; Jonsson, O.; Klatt, B. K.; Pedersen, T. R.; Yourstone, J.; Smith, H. G. Seed coating with a neonicotinoid insecticide negatively affects wild bees. *Nature* **2015**, *521* (7550), 77−80.

(17) Kessler, S. C.; Tiedeken, E. J.; Simcock, K. L.; Derveau, S.; Mitchell, J.; Softley, S.; Stout, J. C.; Wright, G. A. Bees prefer foods containing neonicotinoid pesticides. *Nature* **2015**, *521* (7550), 74−76.

(18) Raine, N. E.; Gill, R. J. Ecology: Tasteless pesticides affect bees in the field. *Nature* **2015**, *521* (7550), 38−40.

(19) Goulson, D.; Nicholls, E.; Botías, C.; Rotheray, E. L. Bee declines driven by combined stress from parasites, pesticides, and lack of flowers. *Science* **2015**, *347* (6229), 1255957.

(20) Hallmann, C. A.; Foppen, R. P. B.; van Turnhout, C. A. M.; de Kroon, H.; Jongejans, E. Declines in insectivorous birds are associated with high neonicotinoid concentrations. *Nature* **2014**, *511*, 341−343.

(21) Forrester, M. Neonicotinoid insecticide exposures reported to six poison centers in Texas. *Hum. Exp. Toxicol.* **2014**, *33* (6), 568−573.

(22) European Union. European commission implementing regulation no. 485/2013. *Off. J. Eur. Communities: Legis.* **2013**, 1.

(23) Brown, M. A.; Petreas, M. X.; Okamoto, H. S.; Mischke, T. M.; Stephens, R. D. Monitoring of malathion and its impurities and environmental transformation products on surfaces and in air following an aerial application. *Environ. Sci. Technol.* **1993**, *27*, 388−397.

(24) World Health Organization. *Pesticide Residues in Food: Evaluations*; WHO: Rome, Italy, 2009.

(25) Wang, L.; Liu, T. Z.; Liu, F.; Zhang, J. J.; Wu, Y. H.; Sun, H. W. Occurrence and profile characteristics of the pesticide imidacloprid, preservative parabens, and their metabolites in human urine from rural and urban China. *Environ. Sci. Technol.* **2015**, *49* (24), 14633−14640.

(26) Moza, P. N.; Hustert, K.; Feicht, E.; Kettrup, A. Photolysis of imidacloprid in aqueous solution. *Chemosphere* **1998**, *36* (3), 497−502.

(27) Redlich, D.; Shahin, N.; Ekici, P.; Friess, A.; Parlar, H. Kinetical study of the photoinduced degradation of imidacloprid in aquatic media. *Clean: Soil, Air, Water* **2007**, *35* (5), 452−458.

(28) Schippers, N.; Schwack, W. Photochemistry of imidacloprid in model systems. *J. Agric. Food Chem.* **2008**, *56* (17), 8023−8029.

(29) Schippers, N.; Schwack, W. Phototransformation of imidaclo-prid on isolated tomato fruit cuticles and on tomato fruits. *J. Photochem. Photobiol., B* **2010**, *98* (1), 57−60.

(30) Scholz, K.; Reinhard, F. Photolysis of imidacloprid (NTN 33893) on the leaf surface of tomato plants. *Pestic. Sci.* **1999**, *55* (6), 652−654.

(31) von Gunten, K. Photodegradation and sorption to Na-SAz clay, soil, and pollen of the neonicotinoids acetamiprid, clothianidin, imidacloprid and thiacloprid. https://www.yumpu.com/en/document/view/7393414/photodegradation-and-sorption-to-na-sazclay-soil-eth-zurich (accessed Sept 15, 2016).

(32) Wamhoff, H.; Schneider, V. Photodegradation of imidacloprid. *J. Agric. Food Chem.* **1999**, *47* (4), 1730−1734.

(33) Wei, Z.; Wei-ping, L.; Yue-zhong, W.; Lee, S.-J. Photochemistry of insecticide imidacloprid: direct and sensitized photolysis in aqueous medium. *J. Environ. Sci.* **2004**, *16* (4), 539−542.

(34) Dell'Arciprete, M. L.; Santos-Juanes, L.; Sanz, A. A.; Vicente, R.; Amat, A. M.; Furlong, J. P.; Martire, D. O.; Gonzalez, M. C. Reactivity of hydroxyl radicals with neonicotinoid insecticides: mechanism and changes in toxicity. *Photochem. Photobiol. Sci.* **2009**, *8* (7), 1016−1023.

(35) Ding, T.; Jacobs, D.; Lavine, B. K. Liquid chromatography-mass spectrometry identification of imidacloprid photolysis products. *Microchem. J.* **2011**, *99* (2), 535−541.

(36) Ding, T.; Lavine, B. K. Separation of imidacloprid and its degradation products using reversed phase liquid chromatography with water rich mobile phases. *J. Chromatogr. A* **2011**, *1218* (51), 9221−9226.

(37) Lu, Z.; Challis, J. K.; Wong, C. S. Quantum yields for direct photolysis of neonicotinoid insecticides in water: implications for exposure to nontarget aquatic organisms. *Environ. Sci. Technol. Lett.* **2015**, *2* (7), 188−192.

(38) Moussa, S. G.; Finlayson-Pitts, B. J. Reaction of gas phase OH with unsaturated self-assembled monolayers and relevane to atmospheric organic oxidations. *Phys. Chem. Chem. Phys.* **2010**, *12*, 9419−9428.

(39) Harrick, N. J. *Internal Reflection Spectroscopy*; Interscience Publishers: New York, NY, 1967; p 327.

(40) Kagabu, S.; Matsuno, H. Chloronicotinyl insecticides 0.8. Crystal and molecular structures of imidacloprid and analogous compounds. *J. Agric. Food Chem.* **1997**, *45* (1), 276−281.

(41) Leighton, P. A.; Lucy, F. A. The photoisomerization of the o-nitrobenzaldehydes I. photochemical results. *J. Chem. Phys.* **1934**, *2* (11), 756−759.

(42) Pitts, J. N.; Wan, J. K. S.; Schuck, E. A. Photochemical studies in an alkali halide matrix. I. An o-nitrobenzaldehyde actinometer and its application to a kinetic Study of the photoreduction of benzophenone by benzhydrol in a pressed potassium bromide disk. *J. Am. Chem. Soc.* **1964**, *86* (18), 3606−3610.

(43) Vichutinskaya, Y. V.; Postnikov, L. M.; Kushnerev, M. Y. The use of o-nitrobenzaldehyde as internal actinometer when studying photo-oxidative breakdown of thin unoriented polycaprolactam films. *Polym. Sci. U.S.S.R.* **1975**, *17* (3), 716−721.

(44) Allen, J. M.; Allen, S. K.; Baertschi, S. W. 2-Nitrobenzaldehyde: a convenient UV-A and UV-B chemical actinometer for drug photostability testing. *J. Pharm. Biomed. Anal.* **2000**, *24* (2), 167−178.

(45) Galbavy, E. S.; Ram, K.; Anastasio, C. 2-Nitrobenzaldehyde as a chemical actinometer for solution and ice photochemistry. *J. Photochem. Photobiol., A* **2010**, *209* (2−3), 186−192.

(46) Cody, R. B.; Laramée, J. A.; Durst, H. D. Versatile new ion source for the analysis of materials in open air under ambient conditions. *Anal. Chem.* **2005**, *77* (8), 2297−2302.

(47) Gross, J. H. Direct analysis in real time—a critical review on DART-MS. *Anal. Bioanal. Chem.* **2014**, *406* (1), 63−80.

(48) Le Questel, J. Y.; Graton, J.; Cerón-Carrasco, J. P.; Jacquemin, D.; Planchat, A.; Thany, S. H. New insights on the molecular features and electrophysiological properties of dinotefuran, imidacloprid and acetamiprid neonicotinoid insecticides. *Bioorg. Med. Chem.* **2011**, *19*, 7623−7634.

(49) Schirmer, J. Beyond the random-phase approximation: A new approximation scheme for the polarization propagator. *Phys. Rev. A: At., Mol., Opt. Phys.* **1982**, *26* (5), 2395−2416.

(50) Dunning, T. H. Gaussian basis sets for use in correlated molecular calculations. I. The atoms boron through neon and hydrogen. *J. Chem. Phys.* **1989**, *90* (2), 1007−1023.

(51) Koslowski, A.; Beck, M. E.; Thiel, W. Implementation of a general multireference configuration interaction procedure with analytic gradients in a semiempirical context using the graphical unitary group approach. *J. Comput. Chem.* **2003**, *24* (6), 714−726.

(52) Shemesh, D.; Gerber, R. B. Femtosecond timescale deactivation of electronically excited peroxides at ice surfaces. *Mol. Phys.* **2012**, *110* (9−10), 605−617.

(53) Shemesh, D.; Lan, Z.; Gerber, R. B. Dynamics of Triplet-State Photochemistry of Pentanal: Mechanisms of Norrish I, Norrish II, and H Abstraction Reactions. *J. Phys. Chem. A* **2013**, *117* (46), 11711−11724.

(54) Lignell, H.; Epstein, S. A.; Marvin, M. R.; Shemesh, D.; Gerber, B.; Nizkorodov, S. Experimental and theoretical study of aqueous cis-pinonic acid photolysis. *J. Phys. Chem. A* **2013**, *117* (48), 12930−12945.

(55) Shemesh, D.; Nizkorodov, S. A.; Gerber, R. B. Photochemical Reactions of Cyclohexanone: Mechanisms and Dynamics. *J. Phys. Chem. A* **2016**, *120* (36), 7112−7120.

(56) Shemesh, D.; Blair, S. L.; Nizkorodov, S. A.; Gerber, R. B. Photochemistry of aldehyde clusters: cross-molecular versus unim-olecular reaction dynamics. *Phys. Chem. Chem. Phys.* **2014**, *16* (43), 23861−23868.

(57) Weber, W.; Thiel, W. Orthogonalization corrections for semiempirical methods. *Theor. Chem. Acc.* **2000**, *103* (6), 495−506.

(58) Socrates, G. Infrared and Raman Characteristic Group Frequencies: Tables and Charts, 3rd ed.; Wiley, New York, 2004.

(59) Finlayson-Pitts, B. J.; Pitts, J. N. *Chemistry of the upper and lower atmosphere: theory, experiments, and applications*; Academic Press: San Diego, CA, 2000.

(60) Ohkura, K.; Seki, K.-i.; Terashima, M.; Kanaoka, Y. Direct photolysis of halopyridines in solutions; generation of the 2-pyridyl cation. *Chem. Pharm. Bull.* **1991**, *39* (12), 3168−3169.

(61) Lavine, B. K.; Ding, T.; Jacobs, D. LC-PDA-MS studies of the photochemical degradation of imidacloprid. *Anal. Lett.* **2010**, *43* (10−11), 1812−1821.

(62) Carbajo, P. G.; Orr-Ewing, A. J. NO_2 quantum yields from ultraviolet photodissociation of methyl and isopropyl nitrate. *Phys. Chem. Chem. Phys.* **2010**, *12* (23), 6084−6091.

(63) IPCC. *Climate Change 2013: The Physical Science Basis, Contribution of Working Group I to the Fifth Assessment Report of the Intergovernmental Panel on Climate Change*; IPCC: Geneva, Switzerland, 2013.

(64) Portmann, R. W.; Daniel, J. S.; Ravishankara, A. R. Stratospheric ozone depletion due to nitrous oxide: influences of other gases. *Philos. Trans. R. Soc., B* **2012**, *367* (1593), 1256−1264.

(65) Tian, H. Q.; Lu, C. Q.; Ciais, P.; Michalak, A. M.; Canadell, J. G.; Saikawa, E.; Huntzinger, D. N.; Gurney, K. R.; Sitch, S.; Zhang, B. W.; Yang, J.; Bousquet, P.; Bruhwiler, L.; Chen, G. S.; Dlugokencky, E.; Friedlingstein, P.; Melillo, J.; Pan, S. F.; Poulter, B.; Prinn, R.; Saunois, M.; Schwalm, C. R.; Wofsy, S. C. The terrestrial biosphere as a net source of greenhouse gases to the atmosphere. *Nature* **2016**, *531* (7593), 225−232.

(66) Rubasinghege, G.; Spak, S. N.; Stanier, C. O.; Carmichael, G. R.; Grassian, V. H. Abiotic mechanism for the formation of atmospheric nitrous oxide from ammonium nitrate. *Environ. Sci. Technol.* **2011**, *45*, 2691−2697.